

# Mechanical and Structural Degradation of $LiNi_xMn_yCo_zO_2$ Cathode in Li-Ion Batteries: An Experimental Study

Rong Xu, Hong Sun, Luize Scalco de Vasconcelos, and Kejie Zhao\*, z

School of Mechanical Engineering, Purdue University, West Lafayette, Indiana 47907, USA

 ${\rm LiNi}_x{\rm Mn}_y{\rm Co}_z{\rm O}_2$  (NMC) is the current choice of cathode for high-performance Li-ion batteries. The structural and mechanical stability of NMC plays a vital role in determining the electrochemical performance of batteries. However, the dynamic mechanical properties of NMC during Li reactions are widely unknown because of the microscopic heterogeneity of composite electrodes as well as the challenge of mechanical measurement for air-sensitive battery materials. We employ instrumented nanoindentation in an inert environment to measure the elastic modulus, hardness, and interfacial fracture strength of NMC of a hierarchical meatball structure as a function of the state of charge and cycle number. The mechanical properties significantly depend on the lithiation state and degrade as the electrochemical cycles proceed. The results are further compared with the properties of bulk NMC pellets. We perform first-principles theoretical modeling to understand the evolution of the elastic property of NMC on the basis of the electronic structure. This work presents the first time systematic mechanical measurement of NMC electrodes which characterizes damage accumulation in battery materials over cycles.

© 2017 The Electrochemical Society. [DOI: 10.1149/2.1751713jes] All rights reserved.

Manuscript submitted September 12, 2017; revised manuscript received October 16, 2017. Published November 2, 2017.

 ${\rm LiNi_xMn_yCo_zO_2}~(x+y+z=1)$  is among the best cathode materials for the electrification of automobile vehicles given its advantages in high capacity, electrochemical stability, and cost effectiveness. <sup>1-4</sup> NMC is formed by partially replacing Co in  ${\rm LiCoO_2}$  by Ni and Mn to achieve the improved electrochemical performance while reducing the material cost. The composition of Ni, Mn, and Co can be largely tuned to optimize the capacity, rate performance, structural stability, and cost of Li-ion batteries. <sup>5,6</sup>

The structural stability is a key factor plaguing the cyclic performance of NMC materials.<sup>7–11</sup> Recent experiments have shown that the class of NMC, albeit of only  $\sim 5\%$  volumetric change upon lithiation, suffers from heavy structural disintegration and mechanical failure after a number of cycles which significantly increase the ionic and electric impedance of batteries. <sup>12–15</sup> Distinct from the conventional form of particle fracture in Si and LiCoO<sub>2</sub> for instance, <sup>16-18</sup> as-synthesized NMC active materials have a hierarchical meatball structure that small primary particles of submicron size aggregate via van der Waals interactions and form secondary particles of tens of micrometers.<sup>19</sup> The interface between primary particles is rather weak and vulnerable to mechanical failure. By tracking the local morphological evolution, we showed that decohesion of primary particles constituted the major mechanical degradation in NMC.<sup>15</sup> Figure 1 illustrates the interrelationships of mechanical, structural, and electrochemical degradation of NMC cathodes. The electrochemical cycle induces damage accumulation, such as cavitation and particle fracture, 12 and deteriorates the mechanical stability of NMC materials. The degradation of mechanical strength promotes the structural decohesion of NMC secondary particles. Consequently, the cracked particles results in the loss of the active materials and capacity fade in batteries. More importantly, the particle disintegration generates extra fresh surface and facilitates surface construction of the resistance layer which inhibits the ionic and electric conduction, reduces the cyclic efficiency, and ultimately leads to the failure of batteries. <sup>10,20–23</sup>

The mechanical properties of NMC used in practical batteries are widely unknown. Experimental characterization of the structural and mechanical stability of NMC is a challenge, partially because of the difficulty of mechanical measurement for air-sensitive battery materials, and partially because of the heterogeneity of NMC hierarchical particles at the micron scale. <sup>24,25</sup> A couple of recent papers reported elastic modulus and hardness of NMC thin films and pellets, <sup>26,27</sup> nevertheless, the mechanical behavior of NMC of a meatball structure, dominated by the interface between the primary particles, largely differs from that of the condensed format of thin films or pellets. Likewise, the fracture toughness (cohesive strength) of the weakly bonded

NMC secondary particles should be much lower than the intrinsic material properties measured in the bulk materials. Further challenges associated with the mechanical characterization of NMC particles include (I) the requirement of the measurement in an inert environment, (II) the local mapping of the highly heterogeneous composite electrodes at the microscopic level, and (III) the dynamic evolution of the chemomechanical properties of electrodes at different states of charge (SOC) and after a number of lithiation cycles – no data is thus far available for complete characterization of the mechanical stability of NMC in the course of Li reactions.

This paper reports a systematic measurement of the elastic modulus E, hardness H, and interfacial fracture toughness  $K_c$  of NMC as a function of the state of charge and cyclic number. We employ instrumented nanoindentation in an inert environment to probe the local mechanical properties of an example LiNi<sub>0.5</sub>Mn<sub>0.3</sub>Co<sub>0.2</sub>O<sub>2</sub> (NMC532, referred as NMC in the following text) electrode. The mechanical properties largely depend on the lithiation state, albeit the layered crystal lattice is maintained during Li insertion and extraction, and further degrade as the electrochemical cycles proceed. We conduct first-principles modeling to understand the variation of the elastic property of NMC at different states of charge. The theoretical results are in good agreement with the experimental measurements. The quantitative results of the elastoplastic (E, H) and interfacial  $(K_c)$  properties of NMC help understanding of the chemomechanical behavior of NMC materials and will aid the design of composite electrodes of enhanced mechanical and structural stability.

#### **Experimental and Computational Methods**

Sample preparation.—Commercial NMC cathodes (MTI Co.) consisting of 94.2 wt% active materials, 3.0 wt% carbon black and 2.8 wt% PVDF are used as the pristine sample. The coating thickness of the NMC cathode is 45  $\mu m \pm 6~\mu m$  and the areal loading is 121 g/m². To remove moisture, as-received electrodes are dried in a vacuum oven overnight at 80°C and then stored in a glove box in dry argon atmosphere (moisture and oxygen levels less than 1.0 ppm) for several days before use. Next, electrodes are assembled into coin cells for electrochemical cycles. The NMC electrode, Li foil, and Celgard-2502 membrane are used as the cathode, anode, and separator in the CR-2032 type coin cells. The electrolyte is composed of 1 M LiPF6 salt dissolved in ethylene carbonate/diethyl carbonate of 1:1 volume ratio (EC/DEC, 1:1, Sigma Aldrich). All assembled cells are placed to rest overnight to ensure complete wetting before electrochemical

Galvanostatic cycling (BT-2043, Arbin) is performed. Cyclic tests are designed to investigate the influence of two major factors, state of charge and cycle number, on the mechanical properties of NMC

<sup>\*</sup>Electrochemical Society Member.

<sup>&</sup>lt;sup>z</sup>E-mail: kjzhao@purdue.edu

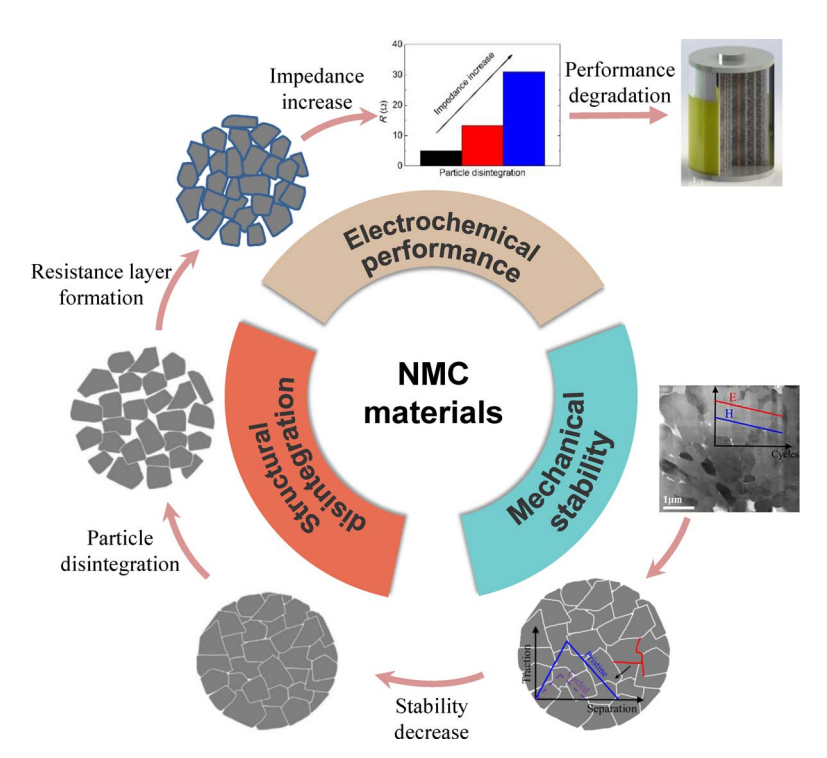


**Figure 1.** Schematics of the mechanical, structural, and electrochemical degradation of NMC cathode materials. Electrochemical cycles induce damage accumulation and deteriorate the mechanical stability of NMC particles. The mechanical degradation promotes the structural decohesion of NMC secondary particles. Consequently, the cracked particles facilitate the formation of resistance layer on the fresh surface which increases the ionic and electric impedance and ultimately leads to the failure of batteries. The cavitation figure is reproduced with permission from Kim et al. <sup>12</sup> Copyright 2016 by Elsevier.

particles. To evaluate the influence of SOC, first batch of cells are charged with C/20 charging rate and 3–4.3 V voltage window until cells reach 33%, 66%, and 100% of SOC, respectively. To examine the effect of cycle number, second batch of cells are initially charged and discharged at C/20, followed by 30, 50, and 100 cycles at C/5 charging rate. After cycles, coin cells are disassembled in the glove box. Cycled NMC electrodes are carefully taken out from the coin cells, washed several times with dimethyl carbonate (DMC, Sigma Aldrich), and dried overnight in a vacuum oven at room temperature.

Both pristine and cycled electrodes are polished (EcoMet 3000, Buehler) before indentation. Samples are mounted on the Al holder and the top surface is polished using micro diamond compounds (LECO Co.). Grit sizes of 3 and 1  $\mu$ m are used for the initial polishing and then 0.05  $\mu$ m colloidal silica suspension is used for final polishing until a mirror-like finish is obtained. Samples are cleaned with isopropyl alcohol after final polishing and delivered into glove box for nanoindentation.

To measure the intrinsic properties of NMC in the bulk form, dense pellets are also prepared. The as-received NMC powders (secondary particles, MTI Co.) are first ball milled into primary particles of submicron size. Then, 2 g of milled powders (primary particles) are pressed into a die (13 mm diameter) under an applied uniaxial compressive stress of 180 MPa (Model 4350, Carvar). Compressed pellets are sintered at 1000°C for 10 h with a heating rate of 10°C/min and are left in the furnace until cooled. As-synthesized NMC pellets are initially polished by silicon carbide sandpaper and then by diamond polishing pads.

*Measurement of E, H, and K<sub>c</sub>.*—The elastic modulus *E*, hardness *H*, and interfacial fracture toughness  $K_c$  are measured using the instrumented nanoindentation (G200, Keysight) in the argon-filled glove box. Targeted indentation<sup>28–31</sup> is performed at the center of the NMC secondary particles of the diameter over 10  $\mu$ m. The maximum impression size is typically less than 1  $\mu$ m, and the distance between the indents and the adjacent matrix is large enough to avoid the influence of the surrounding medium.

E and H are measured with Berkovich indenter using the Oliver-Pharr method. <sup>32</sup> Indentations with maximum indentation load of 1 mN are conducted on 15 different secondary particles in each batch. The loading, holding, and unloading times are 10 s, 5 s, and 10 s, re-

spectively. The load-displacement curves indicate that no detectable cracks are formed during the tests. A series of additional tests are performed to ensure the convergence of the measured results. H is defined as the maximum applied load  $P_{max}$  divided by the contact area A

$$H = \frac{P_{max}}{A_{(h_c)}},\tag{1}$$

where  $P_{max}$  is directly obtained from the prescribed load and the contact area A is calibrated as a function of the contact depth  $h_c$ . Reduced elastic moduli  $E_r$  is derived from the load-displacement response as follows

$$E_r = \frac{S\sqrt{\pi}}{2\beta\sqrt{A}},\tag{2}$$

where S is the slope of the unloading curve upon initial indenter removal and  $\beta$  is a known dimensionless constant that depends on the geometry of the indenter. E is converted from the calculation of  $E_r$ , which takes into account the deformation of both the indenter and sample

$$\frac{1}{E_r} = \frac{1 - v^2}{E} + \frac{\left(1 - v_i^2\right)}{E_i},\tag{3}$$

where Young's modulus and Poisson's ratio of the diamond indenter  $(E_i, v_i)$  are 1141 GPa and 0.07, respectively;<sup>33</sup> and the Poisson's ratio v of NMC is assumed to be 0.3.

Another series of indentations are conducted on the same samples to measure the interfacial fracture toughness  $K_c$ . Cube-corner indenter with a sharp semiapex angle (apical face angle 35.3°) is used to initiate radial cracks between the primary particles. The crack length, the indentation load, and the hardness to modulus ratio are combined to calculate the fracture toughness<sup>34</sup>

$$K_c = \alpha \left(\frac{E}{H}\right)^{\frac{1}{2}} \left(\frac{P}{c^{\frac{3}{2}}}\right), \tag{4}$$

where  $\alpha$  is an empirical constant depending on the geometry of the indenter (0.036 for cube corner indenter) and P is the critical load that generates the crack with the length c. Previous studies have showed that sharp cube corner indenter facilitates crack initiation at much

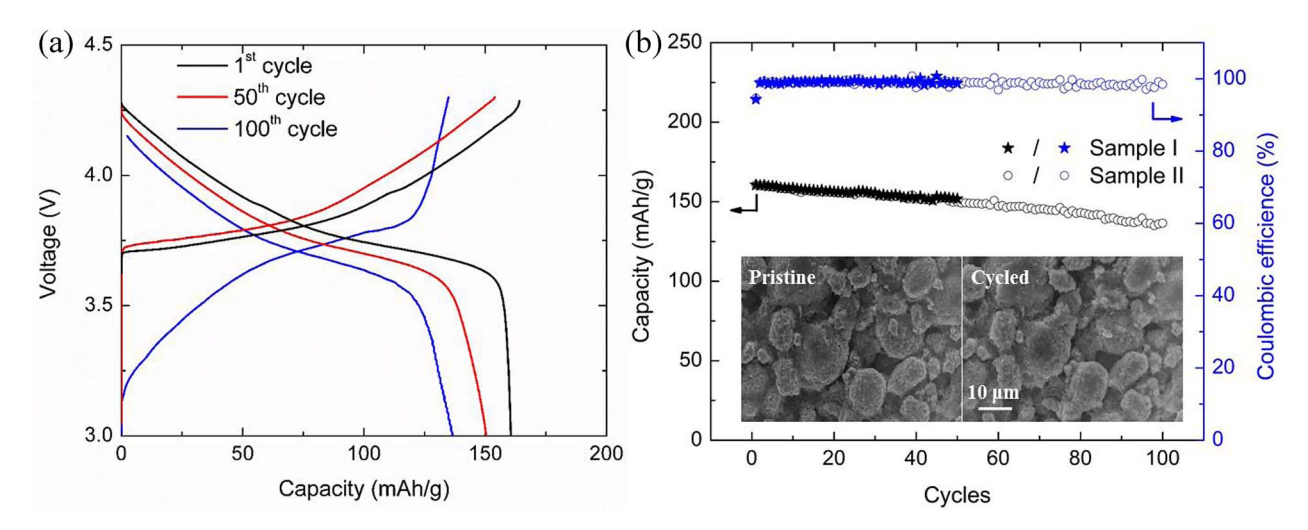


Figure 2. (a) Charge/discharge curves of the NMC/Li half-cell in the 1<sup>st</sup>, 50<sup>th</sup>, and 100<sup>th</sup> cycles. (b) Specific discharge capacity and Coulombic efficiency of NMC cathode as a function of the cycles. Insets show the microstructure of the local regions where indentation tests are performed.

lower loads (e.g., from 0.5 to 1.5 mN) in brittle materials.<sup>35</sup> This advantage allows the fracture toughness measurement of small volumes of brittle materials such as the NMC secondary particles. However, cracks produced at low loads are short and difficult to measure by conventional methods such as optical microscopy and electron microscopy. When brittle materials are indented to generate radial cracks, the load-displacement curve exhibits a sharp increase in the indenter penetration.<sup>36</sup> This sudden increase of indenter penetration is referred as pop-in and is associated with a change of crack morphology. Therefore, the length of indentation-induced cracks can be calculated as<sup>37</sup>

$$c = \sqrt{2}h_m + \left(Q\frac{E'}{H} - \sqrt{2}\right)h_x,$$
 [5]

where  $h_x$  is the pop-in length obtained from the relation  $h_x = h_m - h_t$ ;  $h_m$  is the penetration of indentation with pop-in and  $h_t$  is the anticipated penetration in the hypothetical absence of pop-in, as shown in Figure S1; The values of  $h_m$  and  $h_t$  can be easily obtained from the load-displacement response of indentation tests; E' represents the plane-strain modulus; Q is a material independent constant of 4.55.<sup>37</sup>

The maximum load  $P_{max}$  varies from 1 to 5 mN. The continuity of the load-displacement responses at low loads (1–2 mN), as shown in Figure S1, indicates that there is no detectable pop-in (i.e. crack formation) at this load range. Therefore, they are fitted for the anticipated loading curve in the hypothetical absence of pop-in using a second-order polynomial function. The load-displacement responses with pop-in at higher loads (3–5 mN) are used to calculate the  $h_x$ ,  $h_m$  and c. Post atomic force microscopy (AFM) topography images (Dimension 3100, Veeco Instruments) are acquired to examine the accuracy of the crack length calculated from the pop-in method. Scan size 3.35  $\mu$ m and scan rate 0.5 Hz are used to obtain the height image of the indentation impression, Figure S2. AFM-based crack length is obtained by carefully measuring the distance from indentation center to the crack tip, and then is compared with the crack length calculated from the pop-in method.

*Material characterization.*—The microstructure of NMC is imaged using scanning electron microscopy (SEM, T330, JEOL). The average sizes of NMC secondary and primary particles, Figure S3 a and b, are 10 and 1  $\mu$ m, respectively. The SEM image in Figure S3c shows the surface morphology of sintered NMC pellet where no obvious pores and cracks are present. The fractured surface of NMC pellets in Figure S3d indicates that the average grain size of NMC pellets is around 10  $\mu$ m. X-ray diffraction (XRD) is performed using a diffractometer (D-8 Focus, Bruker) with Cu K-alpha radiation in a 20 range of 12–90° at 100 mA and 40 kV. XRD Bragg peaks of the NMC

electrode as well as the sintered NMC pellets are shown in Figure S3e. The similar XRD patterns confirm that the sintered NMC pellet has same elemental composition as the pristine NMC electrode.

First-principles modeling.—Vienna Ab-initio Simulation Package (VASP)<sup>38,39</sup> is adopted to build the supercell model and simulate the mechanical properties. The NMC supercell is constructed with the R3m space group, where Li, O and TM occupy the 3b, 6c, and 3a sites, respectively. 120 atoms are contained in fully lithiated NMC. The successive delithiated NMC models are constructed by randomly removing a certain number of Li from the LiNi<sub>0.5</sub>Mn<sub>0.3</sub>Co<sub>0.2</sub>O<sub>2</sub> lattice. All NMC models are fully relaxed to achieve the optimized configurations. Projector-augmented wave (PAW) potentials are used to mimic the ionic cores, while the generalized gradient approximation (GGA) in the Perdew-Burke-Ernzerhof (PBE) flavor is employed for the exchange and correlation functional. To model the Coulombic repulsion between localized electrons in transition metals (TMs), the DFT + U method is adopted. The Hubbard U - J values for Ni, Mn, and Co are set as 6.7, 4.2, and 4.91, respectively. 40 The plane-wave set is expanded within an energy cutoff of 520 eV. The  $2 \times 1 \times 1$  mesh of k points in the Monkhorst–Pack scheme is chosen for the Brillouin zone sampling. Energy optimization is considered complete when the magnitude of force per atom is smaller than 0.04 eV/Å. In the supercell model, we apply uniaxial tension in the x, y, and z directions and take the average Young's modulus from the three stress-strain curves.

## **Results and Discussion**

We cycle NMC cathode in half cells and perform nanoindentation of the composite electrodes at given states of charge and after specific cyclic numbers. Figure 2a shows the charge-discharge curves at the 1<sup>th</sup>, 50<sup>th</sup>, and 100<sup>th</sup> cycles by a galvanostatic test of C/5 charging rate and 3–4.3 V voltage window. The corresponding discharge capacities are 160.5, 150.4, and 134.9 mAh/g, respectively. Figure 2b presents the discharge capacity and coulombic efficiency of the coin cells as a function of cycle number. As the cycles proceed, the half cells retain 93.7% and 84.1% of their initial capacity after 50 (sample I) and 100 (Sample II) cycles, respectively. The coulombic efficiency in the initial cycle is 84.3% and remains over 97.5% in the subsequent cycles. The electrochemical behavior of NMC electrodes is consistent with the literature report. <sup>10,41</sup> The SEM images in the inset of Figure 2b show the microstructure of the local regimes where no apparent damages are present and nanoindentation is performed.

NMC samples are polished before nanoindentation to eliminate the influence of surface roughness. The exemplary morphology of a

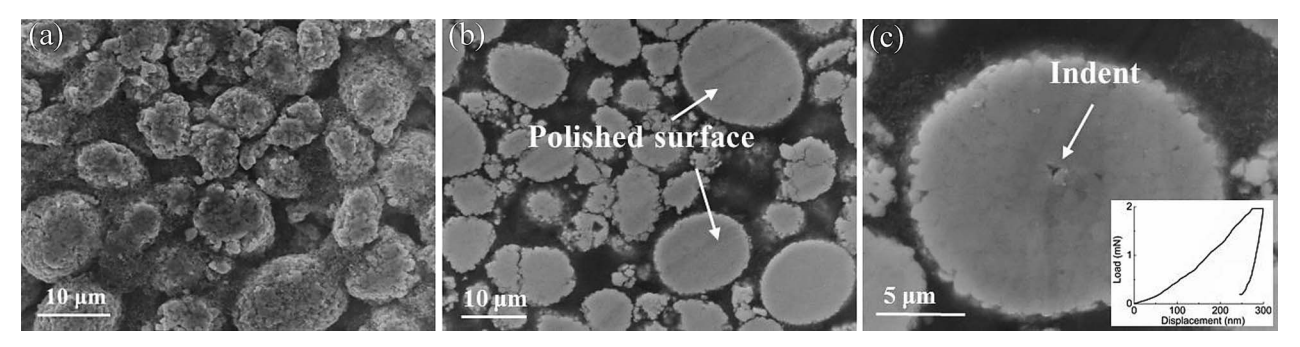


Figure 3. SEM images showing the surface morphologies of the NMC particles (a) before and (b) after polishing. (c) Local view of a NMC secondary particle after nanoindentation. Inset shows the load-displacement response of indentation.

pristine NMC electrode before and after polishing is shown in Figures 3a and 3b. The shape of the NMC secondary particles before polishing is spherical in nature and primary particles are closely packed without obvious gaps in between. After polishing, the packing of primary particles remains intact, and most secondary particles show a flat cross section which suits the indentation. It is worth noting that nanoporosity may exist along the grain boundaries which are inherited from the material synthesis procedure. 12 In the indentation experiments, we select the NMC particles without apparent voids or cracks. Nevertheless, the presence of the microscopic defects is part of the morphological nature of the NMC particles, and their influence on the mechanical strength of NMC is embedded in the experimental results. Figure 3c shows the surface morphology of an indented particle where the indentation site is located at the center of the spherical particle. The impression is much smaller than the particle size. No detectable damage except the impression is observed, Figure 3c. The load-displacement is continuous and is solely determined by the mechanical response of NMC secondary particles as shown in the inset of Figure 3c.

Instrumented nanoindentation is widely used to measure the mechanical properties of bulk materials at small scales.<sup>35</sup> Nevertheless, nanoindentation of composite materials of microscopic heterogeneity remains technically challenging and requires careful calibration. The composite electrodes consist of NMC active particles embedded in a porous matrix of carbon black conductive agents and polymer binders. The constituents have vastly different mechanical properties. Factors influencing the nanoindentation results include (I) the indentation site, (II) the substrate (surrounding matrix) effect, and (III) the applied indentation load. We examine the effect of the above factors by conducting a series of control experiments. We employ targeted indentation with a precise selection of the indentation site to obtain the properties of the single phase of NMC secondary particles in the composite configuration.

We first evaluate the sensitivity of the mechanical measurement on the indentation site. Tests performed near the interface between NMC particles and the surrounding matrix will deviate from the results of pure NMC materials. We measure the elastic modulus E at various locations across two NMC secondary particles of different diameters. The maximum applied load is 1 mN. Figure 4a plots the dependence of E on the normalized position of the indentation site, where 0 and 1 represent the interface between NMC and the matrix, 0.5 represents the center of NMC particles, and values smaller than 0 or larger than 1 represent the matrix regime. As expected, the modulus measured in the matrix is much lower (< 15 GPa) than that within NMC particles ( $\sim$ 145 GPa), and the results close to the interface lie in between these two values. For the regions away from the interface, 0.25 < y/d < 0.75, the measured modulus is consistent and represents the property of pure NMC particles. The blue dashed line dictates the average E measured at the center of 15 different NMC particles which is about 145 GPa. Furthermore, the convergence of E in the two different NMC particles shows the same trend which confirms that the results of targeted indentation are independent of the particle size as long as the indentation site is far away from the interface. We

choose the location of nanoindentation at the center of NMC secondary particles to avoid the interference of the interface and the surrounding matrix.

Next, we examine the substrate effect since the porous conductive matrix is considerably compliant than the NMC particles. We measure the mechanical properties of NMC cathode embedded in two different matrices - one in the conventional mixture of carbon black and PVDF binders and the other in a much stiffer polymer matrix (Phenolic resin, PR). The elastic modulus E and hardness H of PR (10.1  $\pm$  0.8 GPa and  $1.1 \pm 0.2$  GPa, respectively) are one order of magnitude higher than that of the conventional conductive matrix (1.78  $\pm$  0.35 GPa and  $0.043 \pm 0.01$  GPa, respectively). The volume fractions of NMC active particles in the two composites are close as shown in Figure 4b. The red and black columns in Figure 4b show the modulus and hardness of NMC measured in the two matrices - the values are very close,  $E=142.5\pm11.33$  GPa and  $H=8.58\pm1.3$  GPa for NMC in CB+PVDF, and  $E=146.6\pm9.81$  GPa and  $H=8.65\pm1.02$ GPa for NMC in PR. This comparison indicates that the selection of the matrix surrounding and underlying NMC particles has little effect on the indentation results because the indentation depth and the impression size are considerably smaller than the particle size.

The maximum indentation load is another important parameter for the test – a low indentation load sacrifices the experimental accuracy due to the resolution limitation, while a high load may introduce undesired effects of cracking or particle sink-in. We employ both the quasi-static (QS) and continuous stiffness measurement (CSM) methods to find the optimal indentation load. The CSM method allows a continuous measure of the dynamic material stiffness during loading using a low magnitude oscillating force. 42 Figure 4c plots the modulus E measured under different indentation loads. Two regions are identified. In region I, where the indentation load is smaller than 2 mN, E is independent of the applied load and converges to the intrinsic value of NMC secondary particles. In region II, E measured by the QS method monotonously decreases as the indentation load increases. The CSM results show several sudden drops at certain indentation loads. These drops correspond to the formation and propagation of cracks, which are readily induced by indentation in brittle materials. The cracking features are also represented by the pop-in events on the load-displacement curves, as shown in the inset of Figure 4c. The sharp increase of the indenter penetration causes overestimation of the indentation depth and the contact area; therefore the measured values are lower than the intrinsic properties of NMC particles. With further increase of indentation load over 10 mN, E continuously decreases because of interface cracking and particle sink-in which renders the Oliver-Pharr method unsuitable in determining the mechanical properties of the measured samples.<sup>29</sup> Herein we set our maximum applied load to be 1 mN, well below the threshold (2 mN) to induce cracks in the NMC secondary particles.

The elastic modulus E and hardness H of pristine NMC secondary particles are  $142.5 \pm 11.3$  GPa and  $8.6 \pm 1.3$  GPa, respectively. Table I shows the mechanical properties of the NMC secondary particles, sintered NMC pellets, and elastic modulus obtained by first-principles

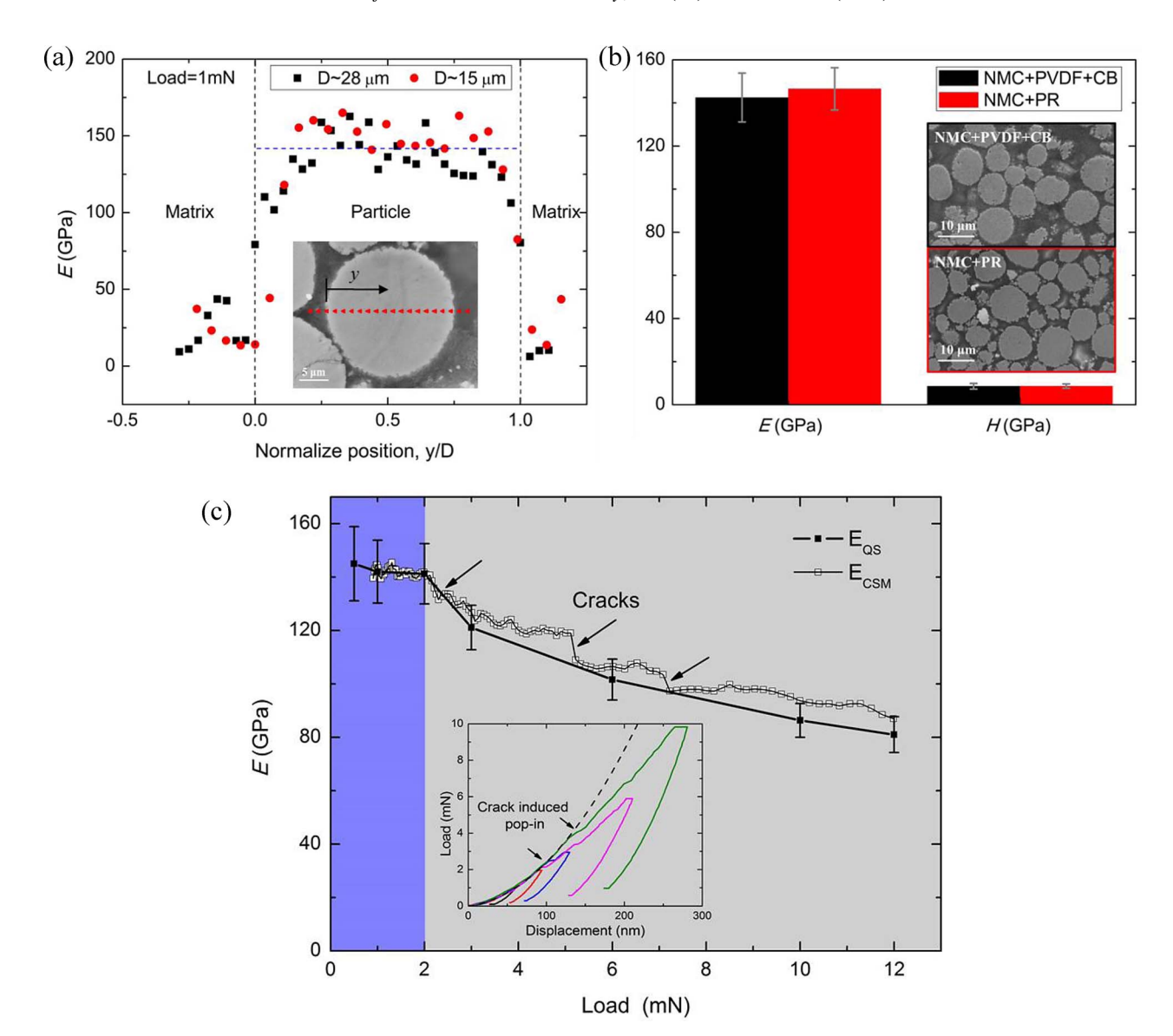


**Figure 4.** (a) Young's modulus *E* measured at different locations across the NMC secondary particles. The measurement is independent of the particle size and the indentation location as long as the indentation sites are away from the particle/matrix interface. (b) Young's modulus and hardness of NMC secondary particles measured in two types of matrixes: PVDF+CB and PR. The small-scale measurement of mechanical properties is insensitive to the selection of the matrix material. (c) Young's modulus of NMC extrapolated from different indentation loads using both the quasi-static and CSM methods. The load-displacement curves in the inset show that the reduction of *E* at high load is due to the cracks induced by indentation.

modeling. Both the modulus and hardness of the NMC segregated particles are considerably lower than that measured in the NMC condensed pellets (177.5  $\pm$  19.5 GPa and 12.6  $\pm$  1.4 GPa, respectively). The pellet measurement and the first-principles result agree well with other reports in recent literature<sup>6,10</sup> and represent the properties of NMC in the bulk form. The lower values of *E* and *H* of NMC sec-

Table I. Experimental values of the mechanical properties of NMC secondary particles and NMC pellets, as well as the theoretical value of Young's modulus obtained by first-principles modeling.

	NMC particles	NMC pellets	First- principles
Modulus E (GPa)	$142.5 \pm 11.3$	$177.5 \pm 19.5$	190.0
Hardness H (GPa)	$8.6 \pm 1.3$	$12.6 \pm 1.4$	N/A
Fracture toughness	$0.102 \pm 0.03$	$0.309 \pm 0.04$	N/A
$K_a  (\text{MPa-m}^{1/2})$			

ondary particles are attributed to the weak interface dictated by van der Waals interactions between primary particles. The size of the nanoindentation impression is around hundreds of nanometers which is comparable with the size of NMC primary particles. The mechanical response of NMC is largely influenced by the "grain boundaries". The interface sliding and defects propagation underneath the indenter significantly reduce the mechanical strength of the NMC composites. Compared to the bulk properties, the behaviors of the segregated particles are more informative on the mechanical and structural stability of NMC electrodes in real batteries.

The mechanical properties of NMC largely depend on the state of charge and degrade as the electrochemical cycles proceed. Figure 5a shows the elastic modulus E and hardness H as a function of SOC during the first delithiation, where 0% represents the pristine NMC and 100% represents  $\text{Li}_{0.5}\text{Ni}_x\text{Mn}_y\text{Co}_z\text{O}_2$ . Delithiation of NMC results in a significant reduction of the mechanical properties. The modulus and hardness of fully charged NMC ( $111.6 \pm 6.4$  GPa and  $7.1 \pm 0.8$  GPa, respectively) are about 77% and 80% of the values for pristine NMC particles. The monotonic decreases of E

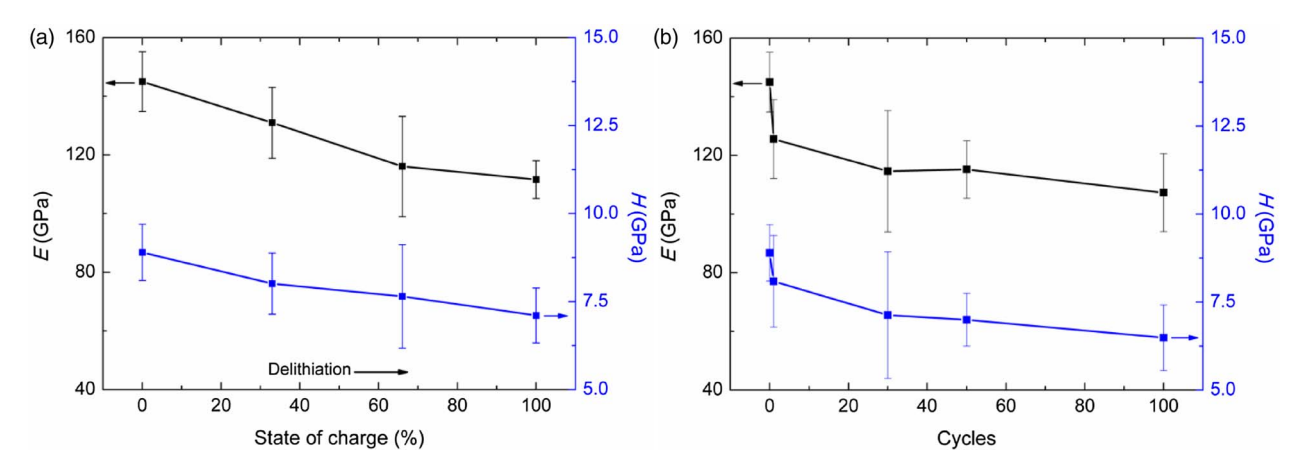


Figure 5. Young's modulus and hardness of NMC secondary particles as a function of (a) the state of charge and (b) cycle number.

and *H* as Li is extracted originate from the reduction of the bonding strength between transition metals (TMs) ions and oxygen. We will discuss this theoretical understanding in detail in the first-principles modeling.

Figure 5b shows the degradation of the mechanical properties of NMC over cycles. The most dramatic reduction of the elastic modulus and hardness occur after the first lithiation cycle. This may be due to the loss of crystallinity of NMC after the initial electrochemical cycle. 12 Complete understanding of the microstructural change associated with early lithiation cycles is to be explored in future studies. After the first cycle, the elastic modulus and hardness of fully lithiated NMC steadily decrease and reduce to  $107.3 \pm 13.3$  GPa and  $6.5 \pm 0.9$ GPa, 74% and 73% of the their initial values in pristine NMC, after 100 cycles. The loss of the mechanical properties over cycles is likely due to the formation and accumulation of nano- and micro-sized voids at the interface between primary particles. Upon electrochemical cycles, the repetitive Li insertion and extraction induce constant volume expansion and contraction. The volumetric change generates mechanical stresses that facilitate the formation of defects concentrated at the grain boundaries. The interfacial defects accumulate and reduce the mechanical strength of the segregated particles while nanoindentation probes. An evidence supporting this scenario is the observation by Kim et al. on the accumulation of damages in the course of lithiation cycles using scanning transmission electron microscopy (STEM). 12 It should be noted that the generation of the nano- or micro-defects does not necessarily cause disintegration of secondary particles or macroscopic damages, however, the population of the defects and interfacial sliding can significantly weaken the overall mechanical performance of NMC secondary particles. The microstructural damage alone may not fully account for the degraded mechanical properties of Li transition metal oxides over cycles.<sup>31</sup> Another factor contributing to the reduction may be due to the atomic structural evolution of NMC upon lithiation cycles. Specifically, when Li ions are extracted from the lattice of a layered structure, the TMs ions of a similar size of Li<sup>+</sup> (mostly Ni<sup>2+</sup>) can occupy the vacant Li sites. This cation mixing results in lattice distortion and thus destabilize the layered structure, leading to the degradation of the mechanical strength of NMC materials.<sup>26</sup> The quantitative mapping of the mechanical properties of NMC on the state of charge as well as the cycle number provide useful input for computational modeling of chemomechanical behaviors of batteries and shed insight on the damage accumulation in NMC materials over cycles.

We understand the evolution of the elastic property of NMC using first-principles theoretical modeling. The electronic structure, Jahn-Teller (JT) structural stability, and atomic bond strength of NMC are analyzed. Figure 6a shows the elastic modulus and the cohesive energy as a function of the state of charge, again 0% represents the pristine NMC, 100% represents Li<sub>0.5</sub>Ni<sub>x</sub>Mn<sub>y</sub>Co<sub>z</sub>O<sub>2</sub>, and the inset figures show the layered atomic configurations. During delithiation,

the Young's modulus of NMC linearly decreases which qualitatively agrees with the experimental result in Figure 5. The quantitative discrepancy originates from the interfacial structure of NMC particles as discussed earlier. Cohesive energy is defined as the energy to break the lattice into isolated free atoms, which represents the strength of atomic bonding and correlates with the elastic property of materials. The cohesive energy shows the similar linearly decreasing trend when Li is extracted. The reduction of the elastic strength of NMC during delithiation is attributed to (I) the Jahn-Teller distortion, (II) the decrease of electrostatic interaction between Li-O, and (III) the reduction of the TM-O polarization. We will discuss each aspect in detail as follows.

The Jahn-Teller distortion destabilizes the crystal lattice and reduces the mechanical strength. When Li is extracted, a fraction of Ni changes the valence state from the inactive JT species Ni<sup>2+</sup> to the active JT ion Ni<sup>3+</sup>, which distorts the octahedral TM-O complex. The probability distribution of Ni-O bond length in Figure S4 and the variation of Bader charge of Ni in Figure S5 both reveal the transition of the oxidation state of Ni. In addition, the increasing fraction of Li vacancy reduces the electrostatic interactions between the Li and the neighboring O layers, resulting in a larger and uneven Li slab distance. Figure S6 shows the increase of the average Li-O bond length and the c-axis lattice parameter during delithiation which indicates the weak electrostatic interactions of Li-O and enhanced repulsion between adjacent anionic O layers induced by Li vacancies. More importantly, the covalent TM-O bonds largely determine the elastic property of NMC. We discussed the detailed TM-O interactions in NMC in an earlier publication. To help our understanding we quote the following brief description. According to the ligand field theory, the interaction between TMs and the ligand (O) is mainly  $\sigma$ -bonding with small contribution of  $\pi$ -bonding in the TM-O octahedral complex. Figure S7 shows an example molecular orbital diagram of the TM complex with the 3d orbital electron population of  $Co^{3+}$  and O 2p orbital. The three degenerated t2g orbitals of transition metals,  $d_{xy}$ ,  $d_{xz}$ , and  $d_{yz}$ , contribute to both the nonbonding and antibonding states. The eg level has a large overlap in the energy scale with the O 2p orbital and constitutes the covalent bonding orbital with a large coefficient for the ligand orbital. The eg\* level is mainly of transition metal d character resulting in the strong anti-bonding interactions. Figure 6b plots the Bader charges of O and TM ions as a function of SOC. When Li intercalates into the NMC lattice (smaller value of SOC), the O Bader charge linearly increases (more negative) while the average TMs Bader charge gradually decreases (less positive). Figure 6c shows the electron transfer between Li and the NMC host. The results are obtained by subtracting the charge density of pristine NMC from that of lithiated NMC. All the atomic positions are assumed to remain unchanged upon Li insertion. The red color represents more electron accumulation. It is clearly seen that Li is completely ionized and gives away nearly all of its valence electrons. The charge transfer

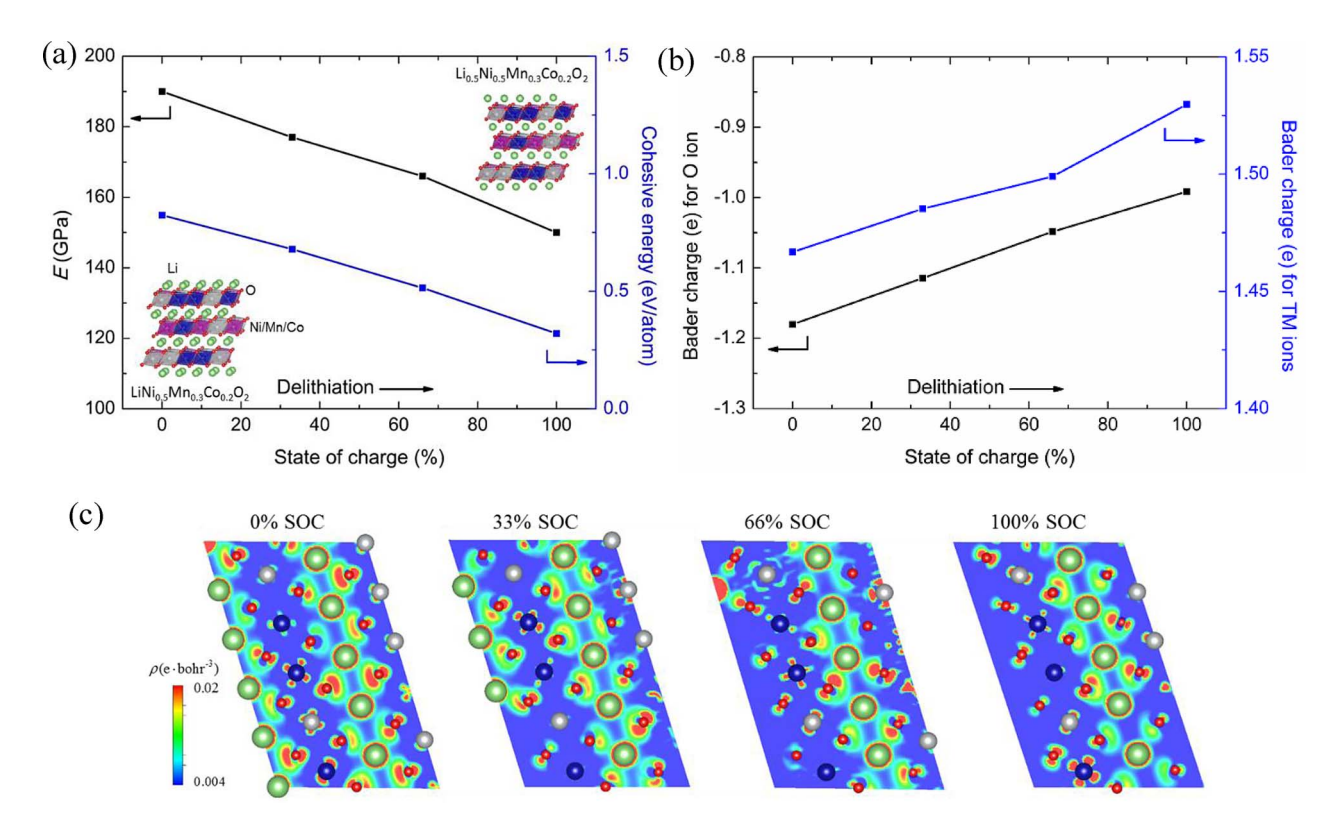


Figure 6. First-principles results on (a) the Young's modulus and cohesive energies, (b) the Bader charge of O and transition metal ions, and (c) the map of electron density difference in NMC at different states of charge.

mainly concentrates on the 2p orbitals of neighboring O ions, as the large red electron cloud is formed nearby the O ions. A small fraction of electrons from Li transfers toward the d orbital (t2g or  $eg^*$ ) of TM ions. The major charge accumulation around O is because of the local electron screening of O ions.  $^{43}$  The large increase of electron density of O 2p orbital makes the  $\sigma$ -bonding of eg orbital in TMs with the 2p orbital of O more polarized and the NMC lattice more ionic in nature. When Li is extracted from the lattice, the TMs-O interactions reduce the polarity and decrease the ionic valence bonding and mechanical strength and NMC.

Next, we measure the interfacial fracture toughness  $K_c$  of NMC secondary particles using cube-corner indenter in a series of indentation experiments. Post AFM topography is employed to analyze the crack patterns within NMC particles after nanoindentation. Figure 7a sketches the interface between primary particles (black dashed lines), radial and lateral cracks (blue lines), and indentation impression (orange lines). The inset shows the AFM image of an indent and a crack of length c. In general, radial cracks readily form at indentation corners and then propagate outward along the radial planes. We observe that radial cracks mostly propagate and deflect along the interface because of the least resistance along the grain boundaries. The NMC primary particles have much larger fracture toughness than the interface. When the indenter is located well within a primary particle, the applied load may not generate radial cracks; instead, it causes ejection of a chip of materials. Previous studies showed that chip ejection in brittle materials is usually associated with lateral cracks (scallop-shape) near or directly beneath the indenter.<sup>37,44</sup> The weak interface in NMC promotes the formation of lateral cracks and chip ejection in primary particles as shown in Figure 7a. Figure S2a and b in the supplementary information show the AFM images of surface morphologies of NMC particles after indentation in which a radial crack of length c and the indentation size of a are marked by the blue and gray arrows. Figure S2c shows the surface height scanning where the red and blue lines in the inset mark the locations of the scans. The

red line regime has a higher surface height owing to the ejection of NMC materials.

The complex fracture modes involving crack deflection and material ejection make the optical measurement of the crack length difficult. Here we employ the pop-in method to calculate the radial crack length  $c.^{37}$  c is determined from Equation 5 (inset in Figure 7b) where the plane-strain modulus E' and hardness H are determined by previous measurements; The pop-in depth  $h_x$  is determined from the loaddisplacement curves with a maximum applied load of 3-5 mN. The hypothetical load-displacement response without any crack formation (dashed line) is a fitting of the load-displacement curve at small loads of 1–2 mN following the Hertzian fitting procedure.<sup>37</sup> Field *el al.* demonstrated that crack deflection or material chipping does not interfere with the calculation of crack length using the pop-in method.<sup>37</sup> We further compare the crack length obtained from the pop-in calculation with AFM imaging. The AFM images give slightly smaller values presumably because of the invisible radial cracks beneath the surface.31

The fracture toughness  $K_c$  is calculated using the radial crack length obtained by the pop-in method, the indentation load, and the hardness to modulus ratio. We conduct 15 indentations on each NMC sample. Among these results, 8-10 indentations are used to calculate the mean values and standard deviations of  $K_c$ , as shown in Figure 8. The rest of experiments showing erroneous load-displacement curves are excluded from the reports. The  $K_c$  for pristine NMC particles, representing the interfacial fracture toughness, is  $0.102 \pm 0.03$  MPa $m^{1/2}$ . This value is three times lower than fracture toughness of sintered NMC pellets which is  $0.309 \pm 0.04$  MPa-m<sup>1/2</sup>. Figure S2 shows the comparison of the load-displacement responses of NMC particles versus pellets. The aggregated particles exhibit a much lower threshold of crack (~ 2 mN) than NMC pellets (> 10 mN). As-synthesized NMC particles clearly have lower structural stability than bulk pellets because of the weak interface joining the primary particles as compared to the inter-grain cohesive strength of the pellets. The fracture

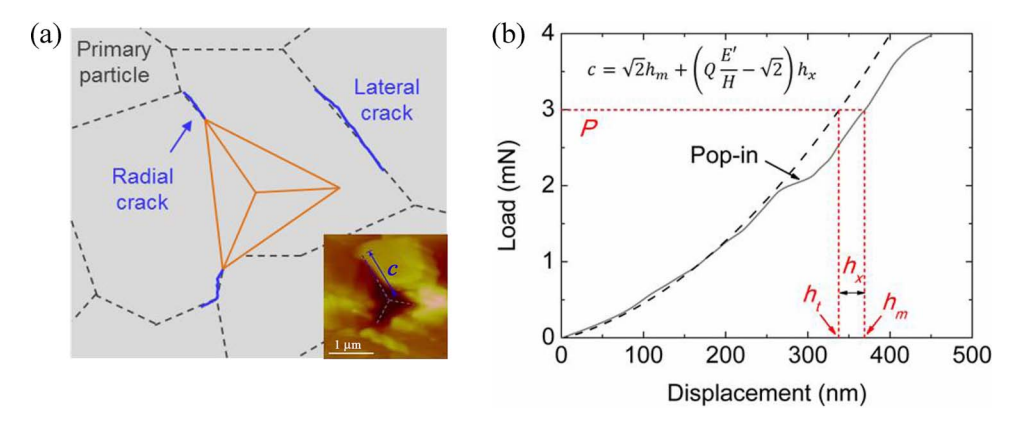


**Figure 7.** (a) Schematics of crack patterns within the NMC secondary particle after nanoindentation. Black dashed, blue, and orange lines represent the interface between the primary particles, the radial and lateral cracks, and the indentation impression, respectively. Inset shows the post AFM image of the indentation impression and the indentation-induced cracks. (b) Load-displacement curve showing the pop-in event and the  $h_x$ ,  $h_m$ ,  $h_t$ , and P in the calculation of  $K_c$ . The pop-in method is validated by comparing the crack length c calculated from the inset equation in (b) with the AFM measurement shown in the inset of (a).

toughness of NMC pellets is close to the reports of other Li transition metal oxides, for instant,  $0.49 \pm 0.13$  MPa-m<sup>1/2</sup> for pristine LiMn<sub>2</sub>O<sub>4</sub><sup>29</sup> and  $0.9 \pm 0.1$  MPa-m<sup>1/2</sup> for LiCoO<sub>2</sub>.<sup>31</sup> It should be noted that grain size of the sintered pellets has a significant effect on the fracture toughness, thus,  $K_c$  of Li transition metal oxides can vary over an order of magnitude depending on the grain size of the sintered pellets.<sup>30</sup> The intrinsic fracture toughness of bulk NMC without any defects should be higher than that measured from the NMC pellets. Prior experiments<sup>45,46</sup> have shown that the grain size affects the nucleation and propagation of intergranular cracks. A larger grain size provides a longer path of fracture propagation and thus decreases the material toughness. We expect that the  $K_c$  of NMC of larger primary particles would show lower interfacial fracture strength. It will be interesting to systematically study the dependence of  $K_c$  of NMC on the grain size in future work.

We proceed to measure the impact of electrochemical cycles on the fracture properties of NMC particles. Figure 8a plots  $K_c$  as a function of state of charge in the first charging (delithiation) process.  $K_c$  exhibits a monotonous decrease upon Li extraction and reduces by nearly a factor of two in  $\text{Li}_{0.5}\text{Ni}_{0.5}\text{Mn}_{0.3}\text{Co}_{0.2}\text{O}_2$ . This reduction of fracture resistance may be caused by residual tensile stresses. Delithiation of NMC is accompanied with a volumetric contraction. The deformation is constrained by the coherence of the grain boundaries and induces a field of tensile stresses within the aggregated particles, which facilitates the formation and propagation of radial cracks during indentation tests. The stress field developed in the course of Li

reactions apparently weakens the interface of primary particles and reduces the integrity of the NMC meatball structure. Figure 8b shows the evolution of  $K_c$  as the electrochemical cycles proceed. Similar to E and H in Figure 5b,  $K_c$  dramatically decreases after the first lithiation cycle. The poor retention of mechanical properties in the early lifetime is attributed to the severe microstructural damages after the first few cycles.  $^{12}$   $K_c$  steadily decreases afterwards and reaches  $0.036 \pm 0.018$  MPa-m<sup>1/2</sup> after 100 cycles – over 60% of the fracture strength is lost compared to the pristine NMC. This dramatic reduction is due to the accumulation of microstructural damages at the interfaces. In the prior STEM study, 12 continuous void expansion and micro-crack generation were observed along the interface as the cycle number increases, primarily induced by the repetitive volumetric change upon electrochemical cycles. The dynamic evolution of the mechanical properties of electrodes in the cyclic life illustrates that the electrochemical practice could significantly deteriorate the structural stability of NMC materials and result in potential catastrophic failure of batteries. It is also interesting to note that the different fracture behaviors of NMC segregated particles versus bulk pellets. While the interfacial fracture toughness of NMC particles is very sensitive to the presence of small-scale defects, Swallow et al. found that the bulk Li transition metal oxides such as LiCoO<sub>2</sub> had minor dependence on the microstructural damages in cycles.<sup>31</sup> This remarkable difference again draws attention on measuring the chemomechanical properties of particles in real batteries which is more informative for the design of enhanced mechanical and structural stability of battery materials.

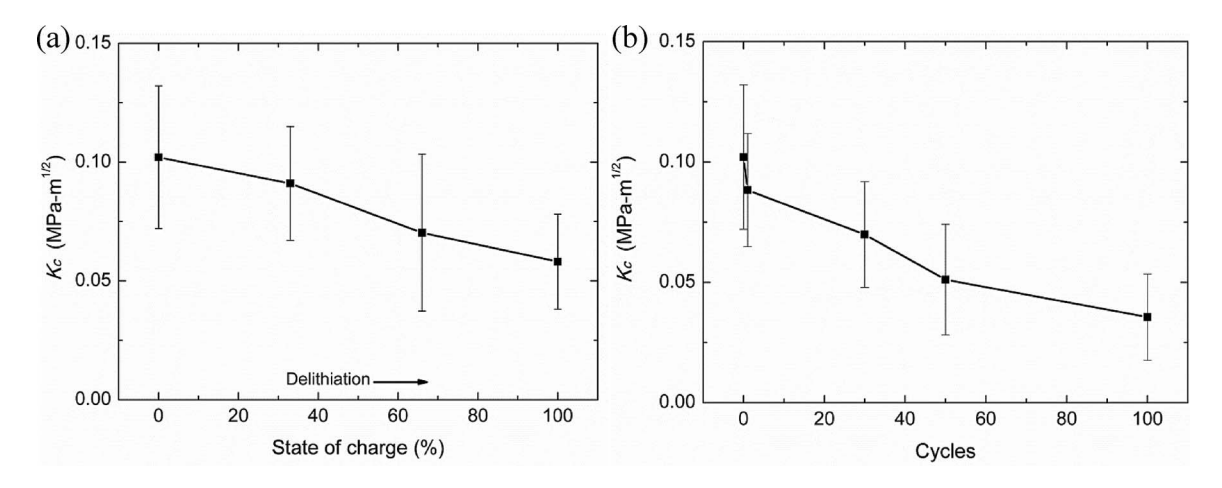


Figure 8. Interfacial fracture toughness  $K_c$  of NMC secondary particles as a function of (a) the state of charge and (b) cycle number.

## Conclusions

We measure the elastic modulus, hardness, and interfacial fracture toughness of NMC particles using instrumented nanoindentation in an inert environment. NMC particles show considerably lower mechanical properties than sintered pellets because of the hierarchical meatball structure. The interface joining the primary particles plays a critical role in determining the mechanical behaviors of NMC cathode materials. We report the dynamic evolution of the mechanical properties as a function of the state of charge and the cycle number. Both the elastic modulus and hardness of NMC largely decrease when Li is extracted from the layered crystalline lattice. First-principles theoretical modeling demonstrates that the reduction of the elastic property of delithiated NMC is attributed to the Jahn-Teller distortion, depletion of electrostatic interactions of Li-O, and charge localization resulted weak ionic TMs-O bonding. The mechanical properties of NMC, in particular the interfacial fracture resistance, significantly decrease as the electrochemical cycles proceed. The loss of mechanical strength is due to the accumulation of microscopic defects and damages at the interface of the constituent primary particles. The experimental results represent the quantitative characterization of mechanical and structural stability of NMC cathode used in real batteries. The output will provide mechanistic understanding on the damage evolution in NMC materials over cycles and offer important insight on the design of composite electrodes of improved chemomechanical performance for high-capacity batteries.

#### Acknowledgments

This work is supported by the National Science Foundation through the grants CMMI-1726392 and CBET-1603866. We are grateful for the help of Biwei Deng for sample preparation, Jiazhi He for AFM imaging, and Qingqing Sun for XRD characterization at Purdue University.

### References

- 1. M. S. Whittingham, Chem. Rev., 104, 4271 (2004).
- 2. P. He, H. Yu, and H. Zhou, J. Mater. Chem., 22, 3680 (2012).
- 3. M. S. Whittingham, MRS Bull., 33, 411 (2008).
- 4. D. Andre, S. J. Kim, P. Lamp, S. F. Lux, F. Maglia, O. Paschos, and B. Stiaszny, J. Mater. Chem. A, 3, 6709 (2015).
- 5. Y. Koyama, I. Tanaka, H. Adachi, Y. Makimura, and T. Ohzuku, J. Power Sources, 119, 644 (2003).
- H. Sun and K. Zhao, J. Phys. Chem. C, 121, 6002 (2017).
- 7. S. Zhang, K. Zhao, T. Zhu, and J. Li, Prog. Mater. Sci., 89, 479 (2017).
- 8. K. Zhao and Y. Cui, Extreme Mech. Lett., 9, 347 (2016).
- 9. R. Xu and K. Zhao, J. Electrochem. Energy Convers. Storage, 13, 030803 (2016).
- 10. G. Li, Z. Zhang, Z. Huang, C. Yang, Z. Zuo, and H. Zhou, J. Solid State Electrochem., **21**, 673 (2017).

- 11. R. Xu and K. Zhao, Extreme Mech. Lett., 8, 13 (2016).
- 12. N. Y. Kim, T. Yim, J. H. Song, J. S. Yu, and Z. Lee, J. Power Sources, 307, 641 (2016).
- 13. M. Lang, M. S. D. Darma, K. Kleiner, L. Riekehr, L. Mereacre, M. Á. Pérez, V. Liebau, and H. Ehrenberg, J. Power Sources, 326, 397 (2016).
- 14. G. Sun, T. Sui, B. Song, H. Zheng, L. Lu, and A. M. Korsunsky, Extreme Mech. Lett., 9, 449 (2016).
- 15. R. Xu, L. S. Vasconcelos, J. Shi, J. Li, and K. Zhao, Exp. Mech., available online (2017).
- 16. X. H. Liu, L. Zhong, S. Huang, S. X. Mao, T. Zhu, and J. Y. Huang, ACS Nano, 6, 1522 (2012).
- 17. X. Hao, X. Lin, W. Lu, and B. M. Bartlett, ACS Appl. Mater. Interfaces, 6, 10849 (2014).
- 18. H. Wang, Y. I. Jang, B. Huang, D. R. Sadoway, and Y. M. Chiang, J. Electrochem.
- 19. L. S. Vasconcelos, R. Xu, J. Li, and K. Zhao, Extreme Mech. Lett., 9, 495 (2016).
- 20. P. Verma, P. Maire, and P. Novak, *Electrochim. Acta*, 55, 6332 (2010)
- 21. N. Liu, Z. Lu, J. Zhao, M. T. McDowell, H. W. Lee, W. Zhao, and Y. Cui, Nat. Nanotechnol., 9, 187 (2014).
- 22. S. Watanabe, M. Kinoshita, T. Hosokawa, K. Morigaki, and K. Nakura, J. Power Sources, 258, 210 (2014).
- 23. D. J. Miller, C. Proff, J. G. Wen, D. P. Abraham, and J. Bareño, Adv. Energy Mater., 3. 1098 (2013)
- 24. M. Ebner, D. W. Chung, R. E. García, and V. Wood, Adv. Energy Mater., 4, 1301278 (2014).
- 25. R. Xu, L. S. Vasconcelos, and K. Zhao, J. Mater. Res., 31, 2715 (2016).
- 26. D. Kim, H. C. Shim, T. G. Yun, S. Hyun, and S. M. Han, Extreme Mech. Lett., 9, 439
- 27. E. J. Cheng, K. Hong, N. J. Taylor, H. Choe, J. Wolfenstine, and J. Sakamoto, J. Eur. Ceram. Soc., 37, 3213 (2017).
- 28. J. Nohava, P. Haušild, Š. Houdková, and R. Enžl, J. Therm. Spray Technol., 21, 651
- 29. H. Y. Amanieu, D. Rosato, M. Sebastiani, F. Massimi, and D. C. Lupascu, Mater. Sci. Eng. A, 593, 92 (2014). 30. M. Qu, W. H. Woodford, J. M. Maloney, W. C. Carter, Y. M. Chiang, and
- K. J. Van Vliet, Adv. Energy Mater., 2, 940 (2012).
- 31. J. G. Swallow, W. H. Woodford, F. P. McGrogan, N. Ferralis, Y. M. Chiang, and K. J. Van Vliet, J. Electrochem. Soc., 161, F3084 (2014).
- 32. W. C. Oliver and G. M. Pharr, J. Mater. Res., 7, 1564 (1992).
- 33. Keysight, G200 User Manual, Rev. G. (2014)
- 34. M. Nastasi, D. M. Parkin, and H. Gleiter, Mechanical properties and deformation behavior of materials having ultra-fine microstructures, Springer, New York (2012).
- G. M. Pharr, *Mater. Sci. Eng. A*, 253, 151 (1998).
  M. V. Swain and J. S. Field, *Philos. Mag. A*, 74, 1085 (1996).
- 37. J. S. Field, M. V. Swain, and R. D. Dukino, J. Mater. Res., 18, 1412 (2003).
- 38. G. Kresse and J. Furthmüller, *Phys. Rev. B*, **54**, 11169 (1996).
- 39. G. Kresse and D. Joubert, Phys. Rev. B, 59, 1758 (1999).
- 40. F. Zhou, M. Cococcioni, C. A. Marianetti, D. Morgan, and G. Ceder, *Phys. Rev. B*, 70, 235121 (2004).
- 41. D. Mohanty, E. Hockaday, J. Li, D. K. Hensley, C. Daniel, and D. L. Wood, J. Power Sources, 312, 70 (2016).
- 42. X. Li and B. Bhushan, Mater. Charact., 48, 11 (2002).
- 43. A. Van der Ven, M. K. Aydinol, G. Ceder, G. Kresse, and J. Hafner, Phys. Rev. B, 58,
- 44. A. Miserez, J. C. Weaver, P. J. Thurner, J. Aizenberg, Y. Dauphin, P. Fratzl, D. E. Morse, and F. W. Zok, Adv. Funct. Mater., 18, 1241 (2008).
- 45. E. Berhardt, B. Stimpson, and D. Stead, Rock Mech. Rock Eng., 32, 81 (1999).
- 46. Y. H. Hatzor and V. Palchik, Int. J. Rock Mech. Min. Sci., 34, 805 (1997).